Research Article Vol. 6, No. 5 / May 2019 / Optica 592

Deep-ultraviolet Smith–Purcell radiation

Yu Ye,[1,2] Fang Liu,[1,2,*] Mengxuan Wang,[1,2] Lixuan Tai,[1,2] Kaiyu Cui,[1,2] Xue Feng,[1,2] Wei Zhang,[1,2,3] and Yidong Huang[1,2,3]

[1]Department of Electronic Engineering, Tsinghua University, Beijing 100084, China
[2]Beijing National Research Center for Information Science and Technology, Beijing, China
[3]Beijing Academy of Quantum Information Science, Beijing, China
*Corresponding author: liu_fang@tsinghua.edu.cn

Received 2 January 2019; revised 21 March 2019; accepted 22 March 2019 (Doc. ID 356241); published 2 May 2019

Smith–Purcell radiation (SPR) is electromagnetic radiation generated by free electrons passing over a periodic grating. Here, having the electron beam pass through 30 nm wide slots in an Al grating greatly shortens the SPR wavelength, and a directional, ultra-broadband, tunable light source spanning $\lambda_0 \approx$ 230–1100 nm is demonstrated. By adjusting the electron energy, backward SPR can be tuned over $\lambda_0 =$ 251–340 nm. This work greatly extends the wavelength of SPR from the previously reported 320 nm to 230 nm, and provides a means of realizing an integrated free-electron broadband light source covering the deep ultraviolet.

https://doi.org/10.1364/OPTICA.6.000592

With the rapid development of nanofabrication technologies, various artificial optical materials/structures with interesting properties have arisen, which promotes research interest in studying the interaction of free electrons with nanoscale structures [1–13]. For example, the acceleration of electrons on a chip [11], the theoretical research of x-ray generation with graphene [12], and on-chip integrated threshold-less Cherenkov radiation [13] were reported. The prospect of on-chip free-electron nano-optoelectronic devices is exciting for various applications. Since uniformly moving free electrons can be treated as an ultra-broadband evanescent electromagnetic field source [14], integrated light sources spanning the ultraviolet (UV) to near-infrared might be realized by extracting the evanescent field into free space.

Smith–Purcell radiation (SPR), first observed in 1953, is the electromagnetic radiation generated by free electrons moving over periodic gratings [15]. Along with synchrotron [16] and cyclotron radiation [17], SPR is an important means of realizing free-electron light sources. For example, the tunable free-electron light source [9], light sources with controlled polarization [18,19], the compact free-electron super-radiant source [20], and lasers in the terahertz region [21,22] are based on SPR. Compared with synchrotron and cyclotron radiation based free electron light sources, SPR-based free-electron light sources are very small and may even be integrated into an integrated optical circuit in the future. SPR in the visible, infrared, and microwave frequency regions has been observed [15,23–27]. However, the shortest wavelength of SPR that has been observed is approximately 320 nm [28]. Further extending SPR into the deep-UV region would be of significance for applications including gas sensing [29], bacteria sterilization [30], and lithography [31].

Here, the free-electron beam passes through nano-slots in two cascaded Al gratings, shortening the wavelength of the SPR into the deep-UV, and an ultra-broadband tunable free-electron light source based on the different diffraction orders of SPR is demonstrated. The radiation spectrum spans $\lambda_0 \approx$ 230–1100 nm. Theoretically, for the configuration employed, the forward SPR spectrum should span $\lambda_0 \approx$ 120–1100 nm (over three octaves). The length of the cascaded gratings (~4 μm) and power consumption (~0.5 mW) are reduced significantly compared with other kinds of broadband light sources [32–37]. Further, by adjusting the electron energy over the range 15–30 keV, the wavelength of SPR in a certain direction could be tuned over a wide range (e.g., $\lambda_0 =$ 340–251 nm).

The Al grating with nano-slots for generating SPR covering the deep-UV is sketched in Fig. 1(a). The electron beam passes through the nano-slots and emits broadband SPR in different directions. In contrast to traditional gratings, the longitudinal nano-slot in the grating enables much stronger interaction between evanescent electromagnetic waves around the electron beam and the grating, especially for SPR in the UV region, which will be discussed in detail with reference to Fig. 2. Figure 1(b) is a scanning electron microscope (SEM) micrograph of the Al grating with nano-slots. The grating was fabricated by sputtering an Al film on a Si substrate and using focused-ion beam (FIB) etching. The thickness, width, and length of the grating are ~150 nm, ~300 nm, and ~2–4 μm, respectively. The actual fabricated nano-slot is trapezoidal with widths at the top and bottom of ~50 nm and ~15 nm, respectively. A schematic of the measurement setup is shown in Fig. 1(c). For SPR measurement, the parameters of the SEM (Zeiss MERLIN

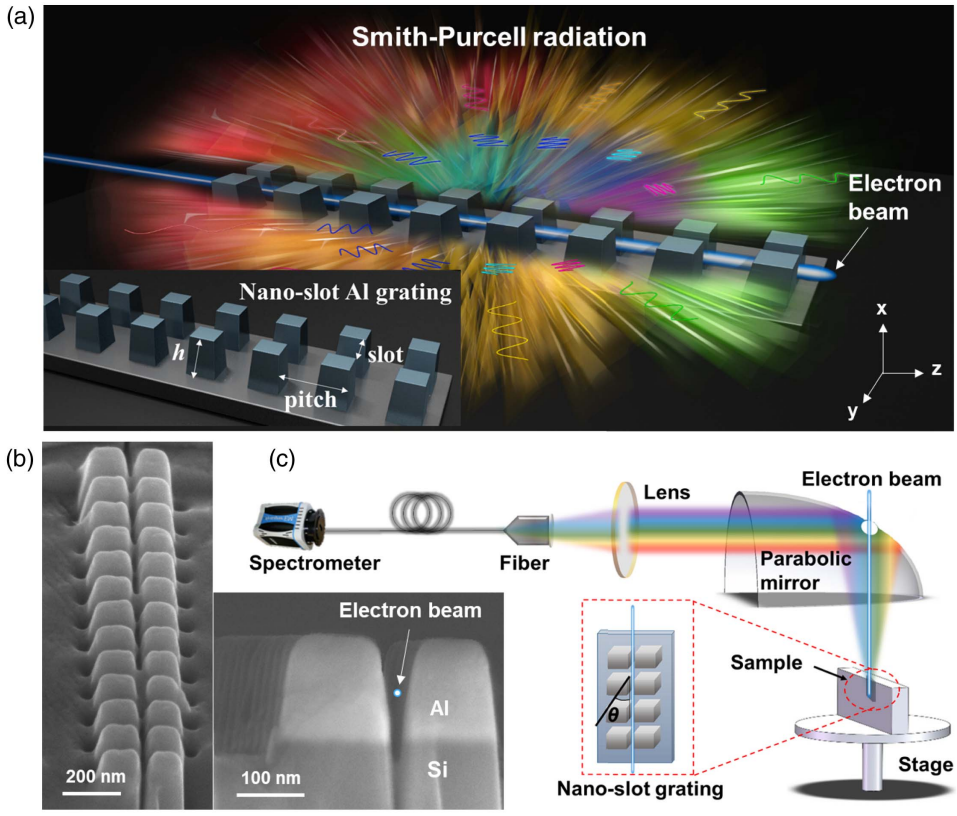

Fig. 1. SPR covering the deep-UV to near-infrared. (a) An electron beam passing through the slot of an Al grating generates a broadband radiation covering the deep-UV to near-infrared. (b) Scanning electron microscope images of the Al grating with pitch of 190 nm. The nano-slot is trapezoid-shaped with bottom width of ~15 nm and top width of ~50 nm. The free-electron beam is precisely controlled to pass through the slot at the position with width of ~30 nm. (c) Schematic of measurement setup based on a cathode luminescence system. The emitted backward ($\theta \approx 180°$) SPR is collected by a parabolic mirror, coupled into a fiber, and detected by the CCD in the spectral range of 200–1100 nm.

field emission scanning electron microscope, Carl Zeiss Microscopy GmbH) are optimized to ensure that the electron beam entering the nano-slot has a diameter (spot size) of ~10 nm, and the angular divergence is ~4–3 mrad with an electron energy of 15–30 keV (the current is 16 nA and electron-source–grating distance is ~6 mm), and a propagation distance of ~6–9 μm is ensured before the beam spot size increases to 30 nm. Thus, after precise alignment, the electron beam passes through the nano-slots of the grating that is less than 4 μm long. The backward ($\theta \approx 180°$) SPR is collected by a parabolic Ag mirror (first surface mirror covered by a high-reflecting film in the UV region), coupled into a conventional fiber, and then detected by a spectrometer with a spectral range of range of 200–1100 nm [see Fig. 1(c)].

The vacuum wavelength λ_0 of SPR is determined by [15,38]

$$\lambda_0 = \frac{L}{m}\left(\frac{1}{\beta} - \cos\theta\right), \tag{1}$$

where L is the pitch of grating, the integer m is the diffraction order, angle θ is the direction of SPR with respect to the direction of the electron beam, and $\beta = v/c$, where v is the electron's velocity (corresponding to electron energy E) and c denotes the velocity of light in vacuum.

According to Eq. (1), by decreasing the pitch of the grating or employing a higher order mode, the wavelength of the SPR can be easily shortened into the deep-UV or even shorter wavelength regions. However, in previous reports when the wavelength of the SPR was shorter than 400 nm, the signal was weak and the shortest wavelength of SPR was about 320 nm [28]. This is attributed to the relatively large gap (g) between the electron beam and the grating. Taking Ref. [9] for example, the gap between electron beam and grating structure is larger than 300 nm. As the evanescent field decays rapidly away from the electron beam, to generate deep-UV SPR with electrons of ≤30 keV energy, the gap should be ≤24 nm (see Section S1 in Supplement 1). Figure 2(a) illustrates the significantly decreased SPR intensity when g is larger than 30 nm, which is in good agreement with Fig. S1(b). This is why SPR with $\lambda_0 < 300$ nm has not been reported.

Having the electron beam pass through the slots of the grating, as shown in Fig. 1, the gap between the electron beam and grating structure is only ~15 nm, ensuring interaction between the evanescent field surrounding the electrons with the grating in the deep-UV region. Moreover, compared with conventional gratings, the nano-slot grating has larger overlap with the evanescent field and generates stronger SPR. Figure 2(b) compares experimentally the SPR generated by the nano-slot grating and a traditional grating with the same pitch (~190 nm) and duty cycle (50%). The electrons pass over the conventional grating with a gap g carefully controlled to ~15 nm, which is almost the same as the gap between the electron beam and the side

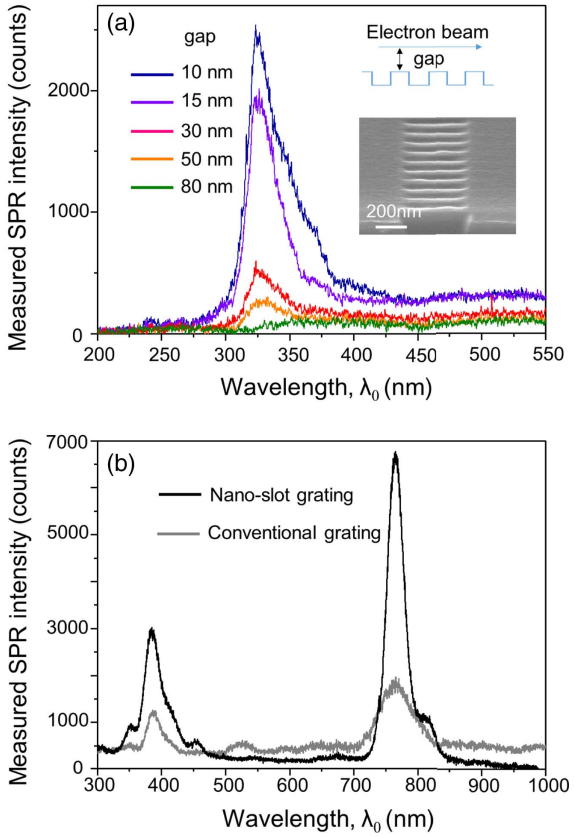

Fig. 2. Key to generating SPR in the UV region. (a) The SPR intensity as a function of the gap g between the electron beam (30 keV) and the conventional grating (pitch 80 nm). Insets are an SEM micrograph of a conventional grating and a schematic showing the gap g. (b) The SPR generated by the grating with a nano-slot (black curve) and conventional grating (gray curve) with the same pitch (190 nm) and electron beam (30 keV, 16 nA).

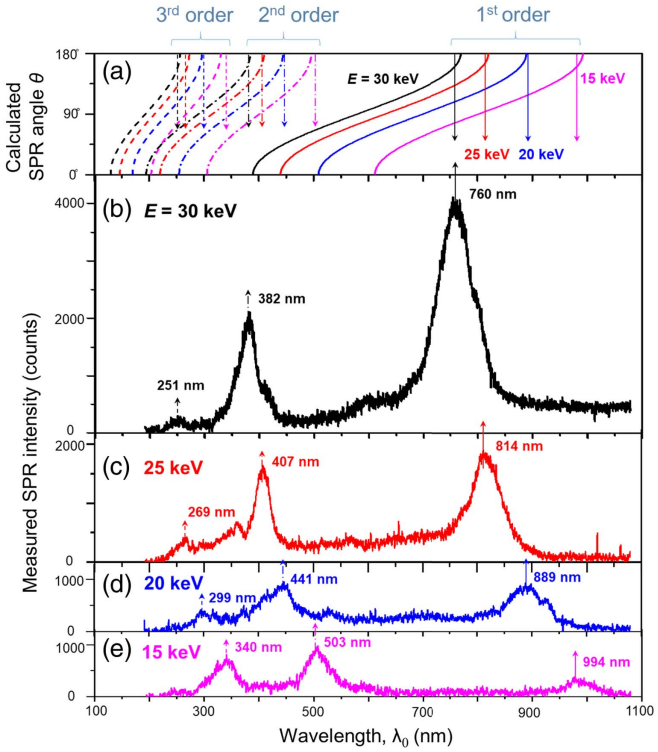

Fig. 3. SPR spectra of a nano-slot grating with a pitch of ~190 nm. (a) The calculated radiation angle θ versus wavelength of SPR according to Eq. (1) for different diffraction orders and electron energies E. (b)–(e) The measured spectra of the SPR at angle $\theta \approx 180°$ for electron energies of 30 keV (black curve), 25 keV (red curve), 20 keV (blue curve), and 15 keV (pink curve). The peak wavelengths of each order marked in (b)–(e) are in good agreement with those in Fig. 3(a) when $\theta = 180°$. Here, the current of the electron beam is fixed at 16 nA. The spectra in Fig. 3 are obtained by subtracting the noise as the electron beam hits the bulk Al directly (see Section S3 of Supplement 1).

wall of the nano-slot grating. The SPR generated by the two structures presents similar spectral profiles and the same peak wavelengths. However, the signal intensity of the nano-slot grating is approximately threefold stronger than that of a conventional grating as a result of the larger overlap of the evanescent electromagnetic field surrounding the free electrons with the grating structure.

For the nano-slot grating with a pitch of 190 nm, Figs. 3(b)–3(e) illustrate the SPR spectra when the electron energy is 30 keV (black curve), 25 keV (red curve), 20 keV (blue curve), and 15 keV (pink curve). It is remarkable that the first-, second-, and third-order SPR could be clearly observed (around the angle $\theta = 180°$) and that SPR with $\lambda_0 < 300$ nm is obtained for the first time. As the electron energy E increases from 15 to 30 keV, the corresponding peak wavelength marked in the figure undergoes a large blueshift (from 994 to 760 nm for the first order; from 503 to 382 nm for the second order; from 340 to 251 nm for the third order). It can be seen that the measured peak wavelengths in Figs. 3(b)–3(e) are in good agreement with Fig. 3(a) (the wavelength at angle $\theta = 180°$) calculated according to Eq. (1). Further, the SPR generated by the nano-slot grating was also simulated and the wavelength and radiation angle [see Fig. S2(a)] also agree well with Fig. 3(a).

Normally, the lower order SPR and larger electron energy E correspond to higher radiation intensity [4,39]. However, for example, the pink curve in Fig. 3(e) indicates that the intensity of the first-order SPR is even weaker than that of both the second and third orders, and larger E corresponds to weaker third-order SPR when comparing Figs. 3(b)–3(e). This is because, compared with the visible light region, the quantum efficiency of the CCD is relatively weak in the range $\lambda_0 < 400$ nm and $\lambda_0 > 800$ nm (see Section S4 in Supplement 1). Further, the deep-UV light is expected to experience a relatively large loss before reaching the CCD via the parabolic mirror, the coupling lens, the fiber, and the wavelength-dependent grating in the spectrometer. Thus, the actual intensity of the near-infrared (800–1100 nm) and UV (200–400 nm) SPR should be higher than that shown in Fig. 2. To increase the intensity of the UV light, the second- or even the first-order SPR could be employed by decreasing the pitch of the grating (see Section S5 of Supplement 1). According to Eq. (1), the SPR has a broadband radiation output at different spatial angle θ. However, in our measurement system as illustrated schematically in Fig. 1(c), only SPR around $\theta \approx 180°$ was collected. The measured output signals of the SPR shown in Figs. 2 and 3 are radiation at $\theta \approx 180°$. If a modified

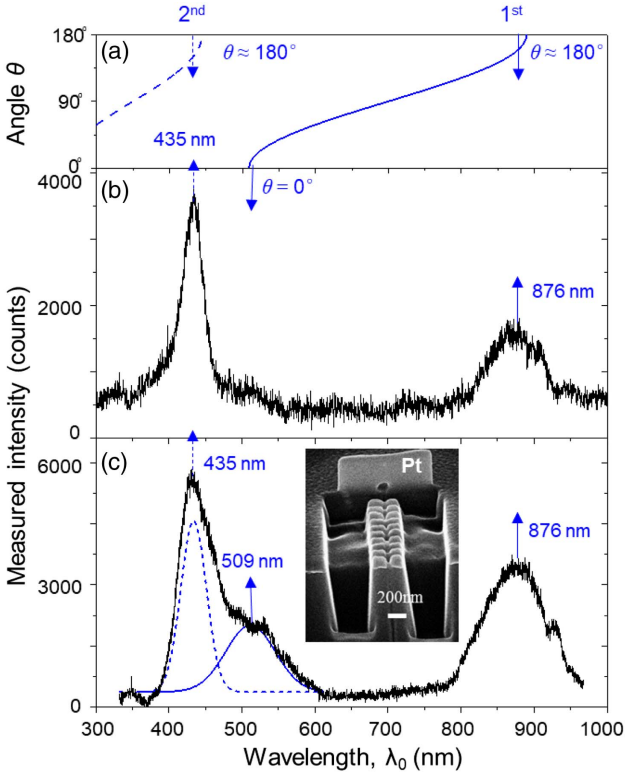

Fig. 4. Observation of forward ($\theta \approx 0°$) SPR. (a) The calculated radiation angle θ versus wavelength of SPR according to Eq. (1). (b) Measured SPR spectrum at $\theta \approx 180°$. (c) Measured SPR spectrum (black curve) with a Pt wall at the end of the grating, which is utilized to reflect the forward ($\theta \approx 0°$) SPR for detection. Solid and dashed blue Gaussian fitting curves correspond to first-order SPR around $\theta = 0°$ and second-order SPR $\theta = 180°$, respectively. Inset shows a SEM micrograph of the grating and Pt wall with an aperture for the electron beam to pass through. Here, the pitch of the grating is ~190 nm and the electron energy is 20 keV.

measurement system is employed [4,40], SPR at other angles with different wavelengths can be observed.

Here we design an experiment to measure the forward SPR at $\theta \approx 0°$, which verifies the broadband SPR output at different spatial angles. As illustrated by the inset of Fig. 4(c), a Pt wall with a height of 1 μm, width of 1.5 μm, and thickness of 300 nm was deposited by FIB at the end of the grating to retro-reflect the forward ($\theta \approx 0°$) SPR for detection, and a hole with diameter of 80 nm was etched in the Pt wall for the electron beam to pass through. Compared with the SPR spectrum without the Pt wall, shown in Fig. 4(b), the measured spectrum with the Pt wall (black curve) in Fig. 4(c) has strong output signal at approximately $\lambda_0 = 509$ nm. The solid and dashed blue Gaussian curves are used to fit the left part of the black curve in Fig. 4(c). It can be seen that the fitting curves agree well with the prediction of first-order SPR around $\theta = 0°$ and second-order SPR $\theta = 180°$ in Fig. 4(a). To exclude other effects (for example, bremsstrahlung and transition radiation) induced by electrons hitting the Pt or passing through the Pt hole, a structure with a Pt wall but no grating was also measured by passing the electron beam through the hole or colliding with the Pt wall. No obvious radiation signal was obtained in these comparison experiments. In addition, considering that the reflected signal around $\lambda_0 = 509$ nm agrees well with Fig. 4(a), forward ($\theta \approx 0°$) SPR could be confirmed.

To realize a wider spectrum and larger radiation intensity in the deep-UV region, a cascaded grating was designed and fabricated using first- and second-order SPR. In Fig. 5(d), the black curve is the SPR ($\theta \approx 180°$) of the cascaded gratings (pitch ~120 nm, length ~1.2 μm; and pitch ~260 nm, length ~2.6 μm) excited by the electron beam with an energy of 30 keV. It is clear that the five peaks of the black curve of Fig. 5(d) are in good agreement with the SPR peaks of the different orders of the two individual gratings [cyan and wine curves in Fig. 5(d)] and the wavelength of SPR at $\theta \approx 180°$ in Fig. 5(a). The simulation results in Fig. 5(c) are also shown for comparison. The simulated SPR at $\theta \approx 145°$ is blueshifted compared with the measurement results in Fig. 5(d), which agrees well with the prediction of Fig. 5(a). The reason for selecting $\theta \approx 145°$ instead of 180° in simulation is to avoid the influence of the evanescent field of the electron beam.

Thus, the directly observed SPR spectrum spans $\lambda_0 \approx$ 230–1100 nm or over two octaves. Limited by the detection range of the CCD, radiation with wavelengths shorter than 200 nm could not be observed directly. However, according to the simulated SPR covering $\theta \approx 0°$–180° illustrated in Fig. 5(b) and the forward SPR indicated by Fig. 4(c), the SPR of the cascaded grating should span $\lambda_0 \approx$ 120–1100 nm or over three octaves, which is a much broader range than previous reports (see Section S6 of Supplement 1). Further, it is easy to extend the spectrum over four octaves by cascading more gratings of different pitches.

The total radiation power of SPR is estimated to be tens of nW for a tens of nA electron beam (see Section S7 of Supplement 1) corresponding to a wavelength range of 230–1100 nm. Considering that the grating area is ~1 μm × 1 μm, the radiation power is several W/cm^2. This is anticipated to be high enough for future biological applications and nano-devices that require relatively low irradiances and are sensitive to heat. For the voltage 30 kV and current 16 nA required to generate SPR in Fig. 5(d), the power consumption of the electron beam is ~0.5 mW. A broadband light source based on SPR generated by cascaded nano-slot gratings requires much less power than the sources reported to date [35–37]. Further, by increasing the current of the electron beam the SPR power could be greatly enhanced (see Section S7 of Supplement 1).

In summary, by passing free electrons through a series of 30 nm wide slots in cascaded Al gratings, the wavelength of the generated SPR is shortened to the deep-UV region and a super-broadband light source spanning over two octaves from the deep-UV to the near-infrared region ($\lambda_0 \approx$ 230–1100 nm) has been realized. Considering the forward SPR, the spectrum should span over three octaves ($\lambda_0 \approx$ 120–1100 nm), and the spectrum can be further extended over four octaves, covering the far-UV to the far-infrared, by cascading more gratings of different pitches. The size of the cascaded grating (150 nm × 300 nm × ~4 μm) is more than 4 orders of magnitude smaller than that of the previous smallest waveguide supercontinuum source [37]. Moreover, the radiation for different wavelengths has different spatial radiation angle, which is convenient for further manipulating the broadband light, and by adjusting the electron energy, the wavelength for a fixed angle θ can be easily tuned over a large

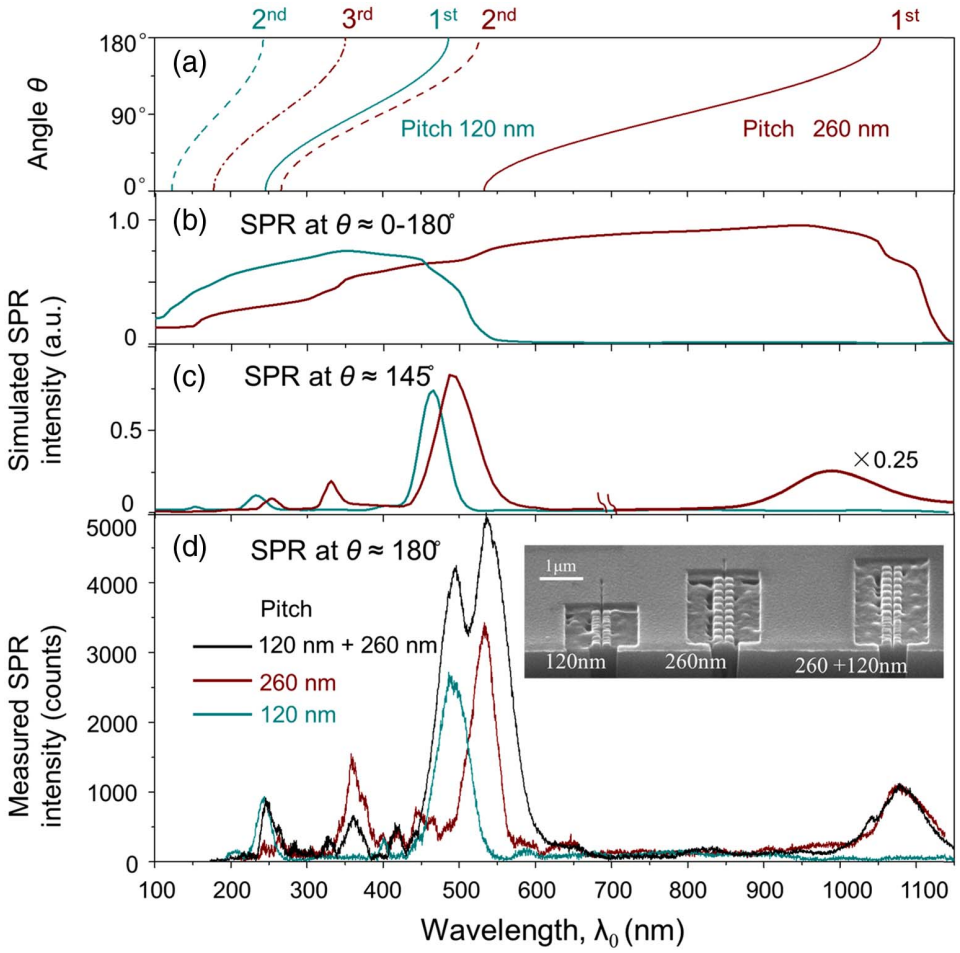

Fig. 5. SPR spectra of cascaded grating with pitch of 120 nm (length 1.2 μm) and 260 nm (length 2.6 μm). (a) The calculated radiation angle θ versus SPR wavelength of the 120 nm and 260 nm pitch gratings. (b), (c) The simulated SPR spectrum covering $\theta \approx 0°$–$180°$ and at approximately $\theta \approx 145°$ with grating pitches of 120 and 260 nm. In Fig. 5(c), the angle 145° was chosen to avoid the influence of the strong evanescent field of the electron beam. (d) The measured SPR spectrum of the cascaded grating (black curve) and two individual gratings (dark cyan and wine curves). Here, the 120 nm pitch grating and 260 nm pitch grating correspond to the dark cyan and wine curves, respectively. The electron energy is 30 keV, the current of electron beam is 16 nA, and the measured radiation angle is $\theta \approx 180°$. The spectra are obtained by deducting the noise as electron beam hits the bulk Al directly.

range (e.g., from 340–251 nm for third-order SPR by adjusting electron energy from 15 to 30 keV).

Funding. This work is supported by National Basic Research Programs of China (2013CBA01704); National Natural Science Foundation of China (NSFC) (61575104, 61621064); and Beijing Natural Science Foundation (Z180012).

Acknowledgment. The authors thank Beijing Innovation Center for Future Chip. The authors also thank Rong Wang and Wenyan Yang of the State Key Laboratory of Tribology, Tsinghua University, and Yunjie Yan and Rong Hu of Beijing National Center for Electron Microscopy for their assistance.

See Supplement 1 for supporting content.

REFERENCES

1. C. Luo, M. Ibanescu, S. G. Johnson, and J. D. Joannopoulos, "Cerenkov radiation in photonic crystals," Science **299**, 368–371 (2003).
2. S. Liu, P. Zhang, W. Liu, S. Gong, R. Zhong, Y. Zhang, and M. Hu, "Surface polariton Cherenkov light radiation source," Phys. Rev. Lett. **109**, 153902 (2012).
3. J. K. So, F. J. García de Abajo, K. F. MacDonald, and N. I. Zheludev, "Amplification of the evanescent field of free electrons," ACS Photon. **2**, 1236–1240 (2015).
4. I. Kaminer, S. E. Kooi, R. Shiloh, B. Zhen, Y. Shen, J. J. López, R. Remez, S. A. Skirlo, Y. Yang, J. D. Joannopoulos, A. Arie, and M. Soljačić, "Spectrally and spatially resolved Smith-Purcell radiation in plasmonic crystals with short-range disorder," Phys. Rev. X **7**, 011003 (2017).
5. Z. Duan, X. Tang, Z. Wang, Y. Zhang, X. Chen, M. Chen, and Y. Gong, "Observation of the reversed Cherenkov radiation," Nat. Commun. **8**, 14901 (2017).
6. Y. Tian, J. Liu, Y. Bai, S. Zhou, H. Sun, W. Liu, J. Zhao, R. Li, and Z. Xu, "Femtosecond-laser-driven wire-guided helical undulator for intense terahertz radiation," Nat. Photonics **11**, 242–246 (2017).
7. M. Gulde, S. Schweda, G. Storeck, M. Maiti, H. K. Yu, A. M. Wodtke, S. Schäfer, and C. Ropers, "Ultrafast low-energy electron diffraction in transmission resolves polymer/graphene superstructure dynamics," Science **345**, 200–204 (2014).
8. T. M. Shaffer, E. C. Pratt, and J. Grimm, "Utilizing the power of Cerenkov light with nanotechnology," Nat. Nanotechnol. **12**, 106–117 (2017).
9. G. Adamo, K. F. MacDonald, Y. H. Fu, C. M. Wang, D. P. Tsai, F. G. de Abajo, and N. I. Zheludev, "Light well: a tunable free-electron light source on a chip," Phys. Rev. Lett. **103**, 113901 (2009).

10. G. Adamo, J. Y. Ou, J. K. So, S. D. Jenkins, F. De Angelis, K. F. MacDonald, E. Di Fabrizio, J. Ruostekosk, and N. I. Zheludev, "Electron-beam-driven collective-mode metamaterial light source," Phys. Rev. Lett. **109**, 217401 (2012).
11. E. A. Peralta, K. Soong, R. J. England, E. R. Colby, Z. Wu, B. Montazeri, C. McGuinness, J. McNeur, K. J. Leedle, D. Walz, E. B. Sozer, B. Cowan, B. Schwartz, G. Travish, and R. L. Byer, "Demonstration of electron acceleration in a laser-driven dielectric microstructure," Nature **503**, 91–94 (2013).
12. L. J. Wong, I. Kaminer, O. Ilic, J. D. Joannopoulos, and M. Soljačić, "Towards graphene plasmon-based free-electron infrared to x-ray sources," Nat. Photonics **10**, 46–52 (2016).
13. F. Liu, L. Xiao, Y. Ye, M. Wang, K. Cui, X. Feng, W. Zhang, and Y. Huang, "Integrated Cherenkov radiation emitter eliminating the electron velocity threshold," Nat. Photonics **11**, 289–292 (2017).
14. F. J. García de Abajo, "Optical excitations in electron microscopy," Rev. Mod. Phys. **82**, 209–275 (2010).
15. S. J. Smith and E. M. Purcell, "Visible light from localized surface charges moving across a grating," Phys. Rev. **92**, 1069 (1953).
16. J. R. Helliwell, "Synchrotron radiation facilities," Nat. Struct. Biol. **5**, 614–617 (1998).
17. J. L. Hirshfield, D. E. Baldwin, and S. C. Brown, "Cyclotron radiation from a hot plasma," Phys. Fluids **4**, 198 (1961).
18. Z. Wang, K. Yao, M. Chen, H. Chen, and Y. Liu, "Manipulating Smith-Purcell emission with Babinet metasurfaces," Phys. Rev. Lett. **117**, 157401 (2016).
19. Y. Yang, C. Roques-Carmes, I. Kaminer, A. Zaidi, A. Massuda, Y. Yang, S. E. Kooi, K. K. Berggren, and M. Soljačić, "Manipulating Smith-Purcell radiation polarization with metasurfaces," in *Conference on Lasers and Electro-Optics* (2018), paper FW4H.1.
20. H. L. Andrews, C. H. Boulware, C. A. Brau, and J. D. Jarvis, "Superradiant emission of Smith-Purcell radiation," Phys. Rev. ST Accel. Beams **8**, 110702 (2005).
21. J. Gardelle, P. Modin, and J. T. Donohue, "Start current and gain measurements for a Smith-Purcell free-electron laser," Phys. Rev. Lett. **105**, 224801 (2010).
22. S. E. Korbly, A. S. Kesar, J. R. Sirigiri, and R. J. Temkin, "Observation of frequency-locked coherent terahertz Smith-Purcell radiation," Phys. Rev. Lett. **94**, 054803 (2005).
23. A. Massuda, C. Roques-Carmes, Y. Yang, S. E. Kooi, Y. Yang, C. Murdia, K. K. Berggren, I. Kaminer, and M. Soljačić, "Smith-Purcell radiation from low-energy electrons," ACS Photon. **5**, 3513–3518 (2018).
24. A. Massuda, C. Roques-Carmes, A. Solanki, Y. Yang, S. E. Kooi, F. Habbal, I. Kaminer, and M. Soljačić, "High-order Smith-Purcell radiation in silicon nanowires," in *Conference on Lasers and Electro-Optics* (2017), pp. JTh5B-8.
25. Y. Yang, A. Massuda, C. S. Roques-Carmes, S. E. Kooi, T. Christensen, S. G. Johnson, J. D. Joannopoulos, O. D. Miller, I. Kaminer, and M. Soljačić, "Maximal spontaneous photon emission and energy loss from free electrons," Nat. Phys. **14**, 894–899 (2018).
26. G. Doucas, J. H. Mulvey, M. Omori, J. Walsh, and M. F. Kimmitt, "First observation of Smith-Purcell radiation from relativistic electrons," Phys. Rev. Lett. **69**, 1761–1764 (1992).
27. Y. Shibata, S. Hasebe, K. Ishi, S. Ono, M. Ikezawa, T. Nakazato, M. Oyamada, S. Urasawa, T. Takahashi, T. Matsuyama, K. Kobayashi, and Y. Fujita, "Coherent Smith-Purcell radiation in the millimeter-wave region from a short-bunch beam of relativistic electrons," Phys. Rev. E **57**, 1061–1074 (1998).
28. J. So, F. M. Kevin, and I. Z. Nikolay, "Fiber optic probe of free electron evanescent fields in the optical frequency range," Appl. Phys. Lett. **104**, 201101 (2014).
29. J. Hodgkinson and P. T. Ralph, "Optical gas sensing: a review," Meas. Sci. Technol. **24**, 012004 (2012).
30. C. C. E. Meulemans, *Ozone Science & Engineering* (Taylor & Francis, 1987), pp. 299–313.
31. C. Wagner and N. Harned, "EUV lithography: lithography gets extreme," Nat. Photonics **4**, 24–26 (2010).
32. R. R. Alfano, *The Supercontinuum Laser Source: The Ultimate White Light* (Springer, 2016).
33. R. D. Saunders, W. R. Ott, and J. M. Bridges, "Spectral irradiance standard for the ultraviolet: the deuterium lamp," Appl. Opt. **17**, 593–600 (1978).
34. J. H. Goncz and P. B. Newell, "Spectra of pulsed and continuous xenon discharges," J. Opt. Soc. Am. **56**, 87–92 (1966).
35. R. Sollapur, D. Kartashov, M. Zürch, A. Hoffmann, T. Grigorova, G. Sauer, A. Hartung, A. Schwuchow, J. Bierlich, J. Kobelke, M. Chemnitz, M. A. Schmidt, and C. Spielmann, "Resonance-enhanced multi-octave supercontinuum generation in antiresonant hollow-core fibers," Light Sci. Appl. **6**, e17124 (2017).
36. X. Jiang, N. Y. Joly, M. A. Finger, F. Babic, G. K. Wong, J. C. Travers, and P. S. J. Russell, "Deep-ultraviolet to mid-infrared supercontinuum generated in solid-core ZBLAN photonic crystal fibre," Nat. Photonics **9**, 133–139 (2015).
37. J. P. Epping, T. Hellwig, M. Hoekman, R. Mateman, A. Leinse, R. G. Heideman, A. Rees, P. J. van der Slot, C. J. Lee, C. Fallnich, and K. Boller, "On-chip visible-to-infrared supercontinuum generation with more than 495 THz spectral bandwidth," Opt. Express **23**, 19596–19604 (2015).
38. A. Gover, P. Dvorkis, and U. Elisha, "Angular radiation pattern of Smith-Purcell radiation," J. Opt. Soc. Am. B **1**, 723–728 (1984).
39. O. Haeberlé, P. Rullhusen, J. M. Salomé, and N. Maene, "Calculations of Smith-Purcell radiation generated by electrons of 1-100 MeV," Phys. Rev. E **49**, 3340–3352 (1994).
40. N. F. Yamamoto, G. A. Javier, and M. Viktor, "Interference of surface plasmons and Smith-Purcell emission probed by angle-resolved cathodoluminescence spectroscopy," Phys. Rev. B **91**, 125144 (2015).